Reaction Chemistry & Engineering

High throughput discovery of ternary Cu-Fe-Ru alloy catalysts for photo-driven hydrogen production

Journal:	*Reaction Chemistry & Engineering*
Manuscript ID	RE-ART-01-2023-000059.R1
Article Type:	Paper
Date Submitted by the Author:	29-Mar-2023
Complete List of Authors:	Bhat, Maya; Carnegie Mellon University, Dept. of Chemical Engineering Simon, Zoe; University of Pittsburgh Talledo, Savannah; Carnegie Mellon University Sen, Riti; University of Pittsburgh, Chemistry Smith, Jacob; University of Pittsburgh, Chemistry Bernhard, Stefan; Carnegie Mellon University, Department of Chemistry Millstone, Jill; University of Pittsburgh, Chemistry Kitchin, John; Carnegie Mellon University, Dept. of Chemical Engineering

Journal Name

ARTICLE TYPE

Cite this: DOI: 00.0000/xxxxxxxxxx

High throughput discovery of ternary Cu-Fe-Ru alloy catalysts for photo-driven hydrogen production†

Maya Bhat,*[a], Zoe C. Simon,[c‡] Savannah Talledo,[b‡] Riti Sen,[c‡] Jacob H. Smith,[c‡] Stefan Bernhard,[b‡] Jill E. Millstone,[c‡] and John R. Kitchin[d]

Received Date
Accepted Date

DOI: 00.0000/xxxxxxxxxx

Light driven hydrogen production from the water splitting reaction has the ability to reduce dependence on fossil fuels in a green energy future. Here, we highlight the discovery of $Cu_xRu_yFe_{1-x-y}$ nanoparticle catalysts for photo-driven hydrogen production. Through a high throughput experimental setup, robust data management pipelines and intentional experimental design, this study uncovered three highly active bimetallic systems for photo-driven hydrogen and identified a new trimetallic catalyst for this system. In most cases, the multimetallic catalysts outperformed the monometallics. This study highlights the expansive catalytic screening capabilities of this system in contrast to traditional catalytic selection processes through the discovery of distributions of particle compositions in binary and ternary mixtures of metals with high activity for hydrogen evolution.

1 Introduction

1.1 Hydrogen Evolution

Clean hydrogen (H_2) production remains an active focus for catalysis research as we move towards greater sustainability in the energy storage and fuel generation space. H_2 can be used in different sectors including heating homes, as a chemical feedstock, and in fuel cell cars.[1–4] Generating hydrogen from renewable sources like water is a process that can have significantly less carbon dioxide emission associated with it than traditional methods from fossil fuels, however this process requires active and stable catalysts[3,5] and carbon-free renewable energy. Though there has been increased research in finding better hydrogen evolution reaction (HER) catalysts, the interest has continued to grow as we look towards a greener future.

HER has been studied in both electrocatalytic and photocatalytic systems. Photocatalysis has some parallels to electrocatalytic systems, and we can use electrocatalytic systems and materials as a reference point for further catalyst development. Photocatalysis is the process of harnessing light energy and using a catalytic surface to drive a chemical reaction.[4,6–8] Though electrocatalysis is a more established field, photocatalysis has gained interest since it can potentially use excess solar energy by direct harvesting of photons from incident light to drive a reaction.[5,6] Light driven HER requires a photosensitizer (PS), sacrificial electron donor, a fuel source, water, and a catalyst.[9,10] Here, we study light driven HER with nanoparticle (NP) catalysts, which are good candidates for HER catalysis since they have high surface area to volume ratios and tunable surface properties.[1,3,11,12] Due to the advantages of both NP as catalysts and growing interest in photo-driven HER, increased attention has been given to this field for photo-driven water splitting.[13–16]

In conventional catalytic studies, the NPs are typically carefully synthesized, isolated and characterized prior to studying their reactivity.[12] This time intensive process can slow the discovery of new materials, especially for materials that pose synthetic challenges or if the materials do not look promising at characterization time (lack of stability, segregation, structural anomalies). In this work we mitigate this issue by synthesizing stable *in-situ* formed NP catalysts while simultaneously assessing reactivity. This *in-situ* synthetic method accelerates the materials discovery process[17–19] and, in this study, led to the discovery of NP catalysts with unanticipated activity. In this study, we use a photo-driven high throughput system to form unsupported colloidal metal catalysts *in-situ* for efficient hydrogen production from water. We focus on Cu, Fe, and Ru, and mixtures of those metals in this work.

[a] *Department of Chemical Engineering, Carnegie Mellon University, 5000 Forbes Avenue, Pittsburgh, Pennsylvania 15213, United States*
[b] *Department of Chemistry, Carnegie Mellon University, 4400 Fifth Avenue, Pittsburgh, Pennsylvania 15213, United States.*
[c] *Department of Chemistry, University of Pittsburgh, 219 Parkman Avenue, Pittsburgh, Pennsylvania 15260, United States.*
[d] *Department of Chemical Engineering, Carnegie Mellon University, 5000 Forbes Avenue, Pittsburgh, Pennsylvania 15213, United States. E-mail: jkitchin@andrew.cmu.edu*

† Electronic Supplementary Information (ESI) available: Additional data supporting the conclusions and information on figure generation. See DOI: 00.0000/00000000.

1.2 Bimetallic and trimetallic nanoparticle systems for HER

In both photo and electrochemical HER, monometallic catalysts have been widely studied.[3,20–25] Numerous studies have shown that Pt and Pd are highly active for HER, however they are expensive and rare.[3,20,26,27] Many efforts have been made to reduce the expensive metal loadings in HER catalysts or replace them altogether.[3,4] Combining metals into multimetallic mixtures or alloys allow for the reduction of one of both metals to attain the same catalytic surface area. Multimetallic catalysts are also a pathway to finding other active materials for HER.[3] When two or more metals mix at an atomic level, their electronic and geometric structures differ from their pure metal components, which impacts their activity, sometimes synergistically, as HER catalysts.[23,28,29] The main challenge with multimetallic systems is that the search space is immense. Not only do the identity of the metals matter, but also their surface configurations, metal loading, particle morphology, and reaction conditions can affect the reactivity. Due to the multidimensional nature of catalyst discovery, finding novel catalysts takes time. With both high-throughput experiments and sophisticated software analytic and modeling tools, this study efficiently screens through multimetallic combinations of Cu, Ru, and Fe for HER.

Monometallic Cu has been studied previously and was shown to consistently produce colloidal NPs upon illumination.[30–32] On its own Cu is not favorable for HER,[33] however studies have suggested an unreactive coinage metal like Cu can enhance the catalytic performance of other transition metal catalysts through alterations in electronic structures..[34,35] Though Cu is immiscible with numerous other transition metals in the bulk phase,[36] some Cu containing bimetallics have been reported to be electrochemically and photocatalytically active for HER.[4,27,35] Additionally, Cu has high electron density, which can help facilitate electron transfer in multimetallic systems.[37]

Ru containing multimetallic NPs are known HER catalysts.[27] Previously, Ru has been shown to enhance Cu reactivity in photo-driven systems from a modeling standpoint,[38] and we hypothesized a similar effect could be experimentally tested here. The combination of Ru and Cu has been electrochemically modeled and experimentally tested, and it has been found to be active for HER.[35,39,40] The CuRu bimetallic has also been studied for HER in metal organic frameworks.[41] Most recently, Cu_xO/RuO_2 have been used as decorating co-catalysts on heterostructures for water splitting photocatalytic applications.[42] Despite bulk immiscibility, prior experiments have suggested the bimetallic could be active for HER with our *in-situ* synthesized colloidal photo-driven system.[36]

Fe was chosen based on its consistent NP formation and high HER activity in prior studies.[17] It is also chemically similar to Ru since it is in the same group as Ru in the periodic table, but it is significantly cheaper and more earth abundant. Similarly to Ru, there have been some electrochemical studies with Cu and Fe containing surfaces that report high HER activity.[37,43] There are also some photocatalytic studies for Cu and Fe with supported NP on graphene and Ni foams that have been active for HER.[44,45] Despite its bulk immiscibility with Cu, it is worth testing Fe in combination with Cu and Ru to assess its feasibility as a colloidal photo-driven HER catalyst.[36]

There are few studies that have looked at Fe and Ru catalysts for HER or the trimetallic combination of Cu, Ru, and Fe. Ternary combinations of these three metals have received some interest, though these previous reports typically involve a bimetallic species and another transition metal or support M (M = TiO_2, Pt, Ag, Co).[46–49] In this work we use a parallel high throughput experimental setup, robust data analytics, and a Design of Experiments (DoE) framework to study the multimetallic combinations of Cu, Ru, and Fe for photo-driven hydrogen evolution with *in-situ* formed colloidal catalysts. This approach allowed us to efficiently investigate the multidimensional space for active HER catalysts and to identify optimal composition regions.

2 Methods

2.1 Experimental

2.1.1 Photocatalytic H_2 Evolution Experiments

Photocatalytic hydrogen evolution experiments were conducted using a home built photo photoreactor capable of running 108 reactions in parallel which has been previously discussed in several publications.[7,8,50] The instrument uses colorimetric detection to monitor experiments with a tape that darkens when hydrogen is present (DetecTape Hydrogen Detection Tape-Midsun Specialty Products, Item DT-H210015-PF4).[8,51] Most reactions were prepared using an automatic liquid dispensing robot (Hamilton Nimbus4), and one well plate was prepared using manual pipettes. The metal salts and iridium photosensitizer (PS = Ir(Fmppy)2dtbbpyPF6 where Fmppy = 4-fluoro-2-phenyl-5-methylpyridine, dtbbpy = 4,4-di-tert-butyl-2,2-bipyridine, synthesized according to literature) solutions were made in DMSO.[52] Poly(ethylene glycol) methyl ether thiol (PEGSH) was used as stabilizing agent for *in-situ* nanoparticles.[32,53] PEGSH and TEOA solutions were made in deionized water, and all reactions were run at a total volume of 440 μL. Images were taken every ten minutes and analyzed using a Wolfram Mathematica program to quantify the amount of hydrogen evolved over the course of 1000 minutes.[7,8,50] Six wells in every well plate contained an internal standard consisting of a photosensitizer, Eosin Y (1 mM, 200 μL), and cobalt (III) bis(BF2-annulated-dimethylglyoxime) pyridine chloride (1 mM, 200 μL) which were added from stock solutions made in methoxyethanol. 20 μL of 60% (w/w) TEOA solution made in water was also added making the total solution volume 420 μL.

2.1.2 Materials

Iron (II) chloride tetrahydrate ($FeCl2 \cdot H_2O$, 99%) and ruthenium (III) chloride hydrate ($RuCl_3 \cdot xH_2O$) were purchased from Sigma Aldrich (St. Louis, MO). Copper (I) chloride (CuCl, 97%) was acquired from Alfa Aesar (Haverhill, MA). Poly(ethylene glycol) methyl ether thiol (PEGSH avg MW = 1 kDA) was bought from Laysan Bio Inc (Arab, AL). Triethanolamine (TEOA, 98%) was obtained from Beantown Chemical (Hudson, NH). These were used without further purification.

2.1.3 Transmission Electron Microscopy (TEM) Experiments

TEM samples were prepared by drop casting an aliquot of the unwashed solution onto a carbon-backed 200 mesh Cu or Ni TEM grid (Ted Pella, Inc.). After drop casting, excess solvent was wicked through the grid, followed by ethanol to remove any remaining DMSO and other reagents. The grids were then dried under ambient conditions and stored under vacuum prior to analysis. A Hitachi H-9500 microscope operating at 300 kV (Nanoscale Fabrication and Characterization Facility, Petersen Institute of Nanoscience and Engineering, University of Pittsburgh, PA) was used for all imaging. Images were analyzed using Digital Micrograph v2.10.1282.0 (Gatan, Inc.) and/or ImageJ v 1.47d (National Institutes of Health, USA) software.

2.1.4 High-Angle Angular Dark Field (HAADF) and Scanning Transmission Electron Microscopy Energy Dispersive X-Ray Spectroscopy (STEM-EDS)

HAADF and STEM-EDS samples were prepared following the same procedure as for TEM analysis then dried under ambient conditions. A probe corrected FEI Titan Themis S/TEM microscope equipped with a Super-X quad EDS detector at 200 kV (NanoScale Fabrication and Characterization Facility, Petersen Institute of NanoScience and Engineering, Pittsburgh, PA) was used for the collection of HAADF images and STEM–EDS elemental maps. Velox 2.13 was used for drift correction during acquisition and data processing. EDS elemental maps were post-filtered using Velox software with a Gaussian blur.

2.2 Computational analysis of results

2.2.1 Screening and Optimization

A high throughput experimental set up for activity screening, characterization studies for identification of synthesized materials, and an iterative Design of Experiments (DoE) framework to rapidly find optimal compositions in multi-variable spaces was used in this work. Each 108 well plate yields data for each well including derived data from image analysis. Due to the inherently multidimensional nature of our experiments, we leverage parallel experimental and computational workflows to explore compositional subsets of both bimetallic and trimetallic combinations of Cu, Ru, and Fe. By coupling the high throughput experiments with an in-house developed software package `gespyranto`,[54] we streamlined the experimental design and data analytics process. The DoE designs employed were response surface and fractional factorial to ensure adequate surveying of the search space and sequential sampling towards optimal regions of activity.[55] It allowed us to digitize the reactor workflow while simultaneously discerning relationships between variables. The confluence of DoE, data processing, and high throughput experimentation was critical to the success and speed of this study.

The experiments were designed with a few constraints. Given the volumetric limit in each well of 440 μL of liquid, there was an upper limit on the amount of metal salt, PS, and ligand that could be studied. Additionally, the limit of hydrogen activity detection before normalization scaling is 2μmol. For this reason, there was poor resolution at very low activities. Finally, there was an upper activity limit of 25 μmol H_2 due to saturation limits of the DetecTape. Staying under 25 μmol H_2 ensured sufficient distinction between highly active wells. The experiments were designed with these constraints in mind.

2.2.2 Activity Metric and Data Normalization

The output data from the experiment are hydrogen evolution time series curves for each well in a plate. The activities in this study are reported as maximum μmol H_2. The maximum μmol H_2 observed in the well is an unambiguous measure of activity and is an easy measurement to take. Measurements like the rate of H_2 production are reliant on derivatives of the time series curves and are prone to errors due to choice of smoothing function, noise and choice of derivative formulas (e.g. forward, centered, etc.). Since the particles are made *in-situ*, the active surface area for HER is unknown - only the initial concentration of metal salt is known. Though the concentrations of metal salts are known, the nanoparticle compositions are not known. As a result, the activity can not be normalized by surface area or particle composition in this work.

The μmol H_2 was normalized by an internal standard measurement and the average Cu activity plate to account for external and internal sources of variation. For each experimental plate, six identical wells containing a molecular catalyst were chosen to be internal standard wells since the molecular species is not subject to particle growth variations and is expected to be more consistent in activity.[8,21] The variation of the internal standard within a plate is less than 2 μmol H_2. The internal standard can capture external uncertainty factors that affect the plate activity such as the intensity of the light bulbs, sensitivity of the detection tape, and temperature in the lab. The internal standard activities and standard deviations can be found in Figure S10. A scaling factor for each plate was used to scale the data across different plates. Some variation due to nanoparticle growth could not be captured with the internal standard. For this reason, the data was also adjusted with a scaling factor reflecting average Cu activity on the plate. Cu was chosen since its HER activity in the system is somewhat independent of concentration, it produces consistent particles, and it was included on all plates included in this study. The Cu averages for each plate can be found in Figure S11. One feature of both of these normalizations is the reported activities are lower than the absolute activities observed on any one plate.

The absolute limit of detection in this system is 2.0 μmol H_2 however after the scaling factors are applied, the averaged scaled limit of detection is 1.1 μmol H_2. The activities will also be expressed as scaled μmol H_2.

3 Results and Discussion

3.1 Monometallics

Before looking at multimetallic combinations, the monometallics of Cu, Ru, and Fe needed to be understood. The monometallic activities of Cu, Fe and Ru were measured and samples from the wells were analyzed by TEM. Figure 1 A, C, and E shows the activities of the monometallics in the order of Cu, Ru, and Fe respectively. The three graphs share the same legend and y axis of scaled μmol H_2. Each data point was repeated at least

three times, and the error bars are the standard deviation of the measurement. A total of 425 data points were used from eight different experiments. The data in Figure 1 A, C, and E contains data from all experimental plates. Each metal was tested at a concentration range from 0 to 0.8 mM metal salt in solution. Figure 1 B, D, and F shows the TEM micrographs of the monometallics in the order of Cu, Ru, and Fe respectively.

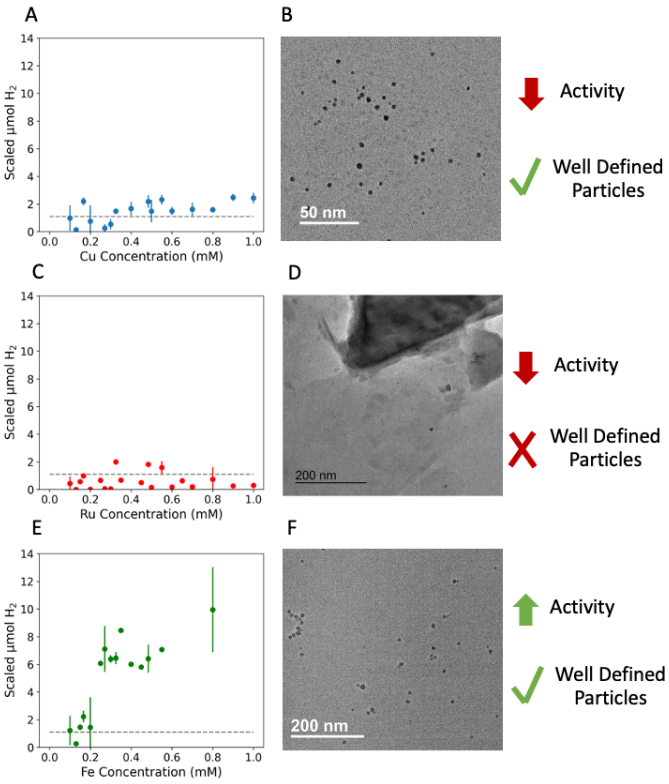

Fig. 1 Monometallic activities and corresponding TEM micrographs. A. Activity of Cu from 0 to 0.8 mM. B. TEM micrograph of Cu sample. Particles are discrete. C. Activity of Ru from 0 to 0.8 mM. D. TEM micrograph of Ru sample. Particles are not well defined and can only be found around organic masses. E. Activity of Fe from 0 to 0.8 mM. The activity increase with increasing concentration of Fe but plateau after 0.3 mM. F. TEM micrograph of Fe sample. Particles are discrete.

The limit of detection is displayed in the activity graphs as a grey dotted line. As seen in Figure 1 A and C, and based on the scaled limit of activity detection of 1.1 μmol H_2, the Ru monometallic sample is inactive for HER and the Cu monometallic sample has low activity for HER. Unlike Cu and Ru, the Fe activity in Figure 1 E consistently performs above the scaled 1.1 μmol H_2 limit of detection and increases with concentration. The monometallic activities observed are consistent with our previous reports.[17]

Figure 1 B, D, and F show the TEM images of the monometallics in the order of Cu, Ru, and Fe respectively. The particles in Figure 1 B and F are discrete consistent with the formation of colloidally stable NPs and the results of our previous study.[17,18] The particle formation is consistent with prior studies where Cu made metallic nanoparticles, and Fe made Fe sulfide particles.[17] The size histograms for the Cu 0.6 mM and Fe 0.8 mM samples can be found at Figure S1 B and S1 D respectively. For Ru in Figure 1 D, it was challenging to locate discrete particles during TEM analysis, and any that were observed were found around masses of organic material.

3.2 Bimetallics

3.2.1 HER Activities

Three bimetallic systems were analyzed, CuRu, CuFe, and RuFe, and tested for HER activity using a variety of molar concentrations and mole fractions. The graphs in Figure 2 clearly show that wells containing combinations of Cu, Ru, and Fe are active for HER. Again, the dotted line is the scaled activity limit of detection at 1.1 μmol H_2. The size of the data points corresponds to total metal loading where the larger points have a higher metal salt concentration, and small points have a smaller metal salt concentration. The x axis for all of the graphs are mole fraction of one of the two metals graphed where the pure metals either lie at $x = 0$ or $x = 1$. The y axis is in scaled μmol H_2.

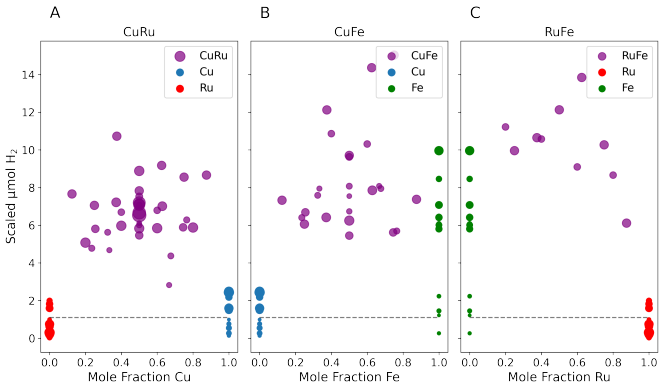

Fig. 2 A. Activity of Ru (red), Cu (blue), and CuRu (purple) wells. CuRu has consistently high activity, whereas the monometallic systems show low activity. B. Activity for Cu (blue), Fe (green), and CuFe (purple) wells. The CuFe shows activity is consistently higher than pure Cu, and has a similar activity to pure Fe. C. Activity for Fe (green), Ru (red), and RuFe (purple) wells. The RuFe activity is high.

Figure 2 A shows the binary combination of Cu and Ru in a well is highly active, despite both pure metals having low activity. This finding suggests there is a synergistic interaction between Cu and Ru that is favorable for HER. In the case of CuFe in Figure 2 B, the CuFe samples are highly active with a few points surpassing the Fe activity. Because both Fe and CuFe have high activities, the potential synergistic interactions between Fe and Cu are less clear. Though wells containing both Cu and Fe are on average more active than wells containing both Cu and Ru, the high activity could be coming from Fe particles or some combination of Cu and Fe. Similarly with RuFe in Figure 2 C, both RuFe samples and pure Fe are highly active, while pure Ru is inactive. To decouple the bimetallic activity to the pure metal activity in these samples, a synergistic analysis was performed.

3.2.2 HER Synergies

In a multimetallic system, one way to identify whether an interaction is occurring or not is by evaluating synergy. Synergy in this

case will be defined as whether the activity of the combination of multiple metals is different from the sum of activities of the pure metals at their respective concentrations. The synergy equation is below where $[M_i]$ is the concentration of pure metal i, $[M_j]$ is the concentration of pure metal j, and $[M_i],[M_j]$ is the bimetallic combination of the two concentrations where i is not j. By this definition we can have positive or negative synergy. This equation can be easily adapted for the trimetallic as well.

$$\text{Synergy} = MaxH_2([M_i],[M_j]) - \sum_i^n MaxH_2([M_i])$$

The pure metals should all have synergies of 0 and any other point equates to the amount of H_2 produced adjusted by the H_2 produced from its corresponding pure metal components. This measurement indicates constructive or destructive multimetallic interactions. The positive data points are points where the bimetallic combinations favorably alter the activity for HER. It was not possible in this work to determine why there is modified activity; it may be due to an increase in active surface area or due to the creation of sites that are more active. The negative data points are where the bimetallic combination under performs. This may be due to surface alterations that lead to poisoning, lower activity, or lower surface area.

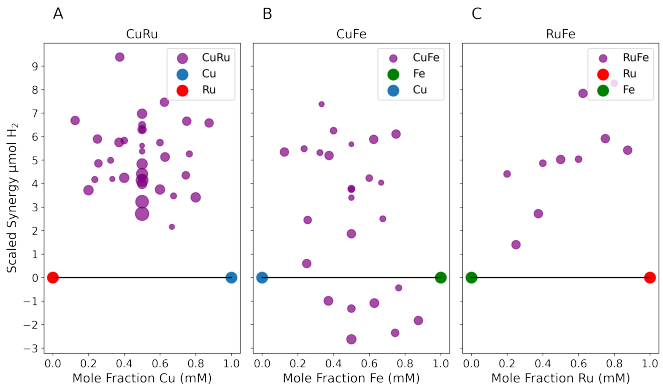

Fig. 3 A. Synergy for Cu and Ru containing wells with Ru (red), Cu (blue), and CuRu (purple). Cu and Ru consistently produces more H_2 together than the sum of their individual components as depicted by the positive synergies. B. Synergy for Cu and Fe containing wells with Cu (blue), Fe (green), and CuFe (purple). CuFe produces both positive and negative synergies. C. Synergy for Ru and Fe containing wells with Fe (green), Ru (red), and RuFe (purple). RuFe consistently produces positive synergies.

Figure 3 shows the synergies of different compositions in the bimetallic composition spaces. The size of the data point represents the total amount of metal in the wells. Pure metals are shown at mole fraction of 0 and 1. Figure 3 A shows the synergy of CuRu. CuRu consistently shows positive synergies which indicate that CuRu is producing more H_2 than the pure metals. Since both Cu and Ru are relatively inactive on their own, this is particularly exciting, especially since these metals are known to be immiscible in the bulk phase. Figure 3 B shows the synergy of CuFe. Unlike CuRu, CuFe has some negative synergies. The particles with larger total metal concentrations seem to be the ones with negative synergies. One possibility for this is that since Cu is easily reduced, at higher mole fractions and concentrations of Cu, the electrons may go towards reducing Cu^{2+} instead of Fe^{2+} or H^+. The competing reactions with e^- as the limiting reactant may be the result of this lower H_2 activity. Figure 3 C is the synergy for RuFe. RuFe has positive synergies that appear to increase with Ru concentration.

3.2.3 Characterization of bimetallic well contents

Each of the most active bimetallic compositions, as determined by DoE driven optimization, were characterized by TEM, HAADF, and STEM-EDS. Because the particles were formed in-situ, the chemical composition of the particles is unknown without further characterization, even though we know the initial solution composition. TEM was performed as an initial characterization to determine whether nanoparticles were formed during the experiment. Prior studies indicate the HER activity in this system is usually driven by heterogeneous NP catalysts.[7,18] TEM micrographs also confirm the presence of stable colloidal nanoparticles. STEM-EDS provides insight into the chemical composition of particles and was performed for each bimetallic sample. STEM-EDS mapping provides insight into the stoichiometry and chemical ordering of the particles present determined by TEM. The results are summarized in Figure 4.

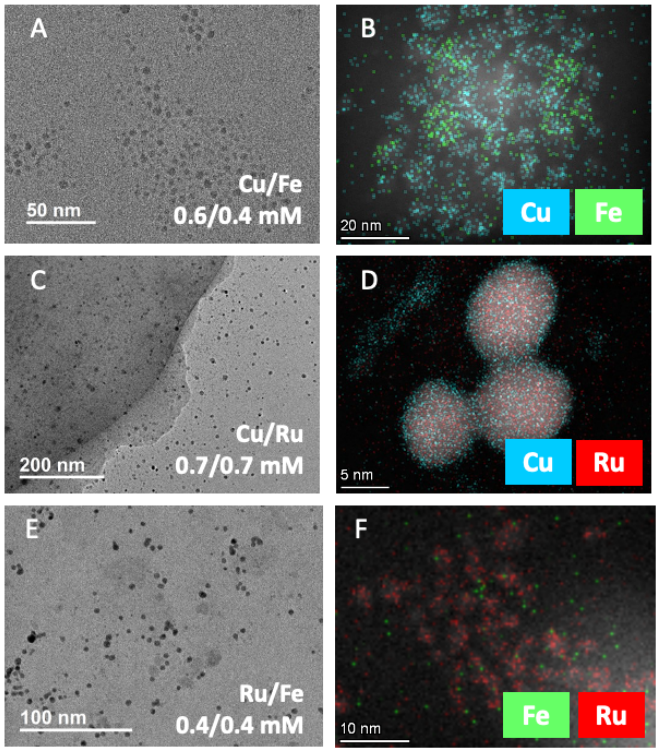

Fig. 4 A. TEM micrograph of 0.6 mM Cu and 0.4 mM Fe sample showing the formation of discrete particles. B. STEM-EDS map of a CuFe sample showing two particle populations: Cu monometallic particles and CuFe bimetallic particles. C. TEM micrograph of 0.7 mM Cu and 0.7 mM Ru sample showing the formation of discrete particles. D. STEM-EDS map of a CuRu sample showing core-shell CuRu-Cu NPs. E. TEM micrograph of 0.4 mM Ru and 0.4 mM Fe sample showing the formation of discrete particles. F. STEM-EDS map of a RuFe sample showing two particle populations: Ru monometallic particles and bimetallic RuFe particles. Size histograms for each sample can be found in Figures S2-S4. STEM-EDS linescans for each sample or samples of similar morphology can be found in Figures S6-S8.

The CuFe samples have discrete particles as shown in Figure 4 A at 0.6 and 0.4 mM concentrations of Cu and Fe respectively (this finding was also observed at lower metal concentrations, TEM micrographs and corresponding size histograms can be found in Figure S2). In Figure 4 B, the presence of both Cu monometallic particles and CuFe bimetallic particles were observed. The linescans of the CuFe sample can be found in Figure S6 B and confirm populations of both Cu monometallic particles and CuFe bimetallic particles.

The CuRu particles are discrete at 0.7 mM and 0.7 mM concentrations of Cu and Ru as shown in Figure 4 C. Size histograms for these particles and similar composition samples can be found in Figure S3. STEM-EDS analysis determined the presence core-shell particles consisting of a CuRu bimetallic core with a Cu shell. In addition to the CuRu particles, additional Cu containing species were observed as indicated in the top right of Figure 4 D. These species primarily contain Cu with small amounts of Ru. The linescans for the sample with 0.5 mM Cu and 0.5 mM Ru can be found in Figure S7 B.

The RuFe samples are discrete at 0.4 mM and 0.4 mM concentrations of Ru and Fe as shown in Figure 4 E. Size histograms for these particles and similar composition samples can be found in Figure S4. The STEM-EDS map in Figure 4 F, determined the presence of both Ru and Fe in the sample. Linescans in Figure S8 B confirm there are populations of both Ru monometallic particles and RuFe bimetallic particles. This result was unexpected because the Ru monometallic samples did not as readily form discrete particles (Figure 1 D). In contrast, Fe monometallic samples did form discrete particles (Figure 1 F). When combined, however, Ru has a significantly higher signal than Fe. Both Ru monometallic and RuFe bimetallic populations are present in the sample. Due to the absence of Fe monometallic particles, the HER activity from this sample is due to either the RuFe bimetallic or Ru monometallic particles.

3.3 Trimetallics

3.3.1 Activities and Synergy

The ternary system was tested with Cu, Ru and Fe at a total metal loading of 0.8 mM. 0.8 mM was chosen as the total metal loading since it is high enough to ensure a distribution of activities and it is low enough to ensure the system is not limited by the availability of the charge carrying photosensitizer. Initial experiments also uncovered that at concentrations around 0.8 mM total metal concentration there were both positive and negative synergies for the bimetallics. The activity and synergy for the ternary system is shown in Figure 5.

The ternary activity and synergy plots have monometallics in the corners with pure Fe in the bottom left corner, pure Cu in the bottom right corner, and pure Ru in the top corner. Similar to the dedicated monometallic data, Fe is active and Cu and Ru are not active. Along the bottom axis is the binary mixture of Cu and Fe wells. The right axis is the binary mixture of Cu and Ru, and the left axis is the binary mixture of Ru and Fe. The points in the middle are the ternary combination of the three pure metals. It is clear from Figure 5 A that at lower Fe concentrations

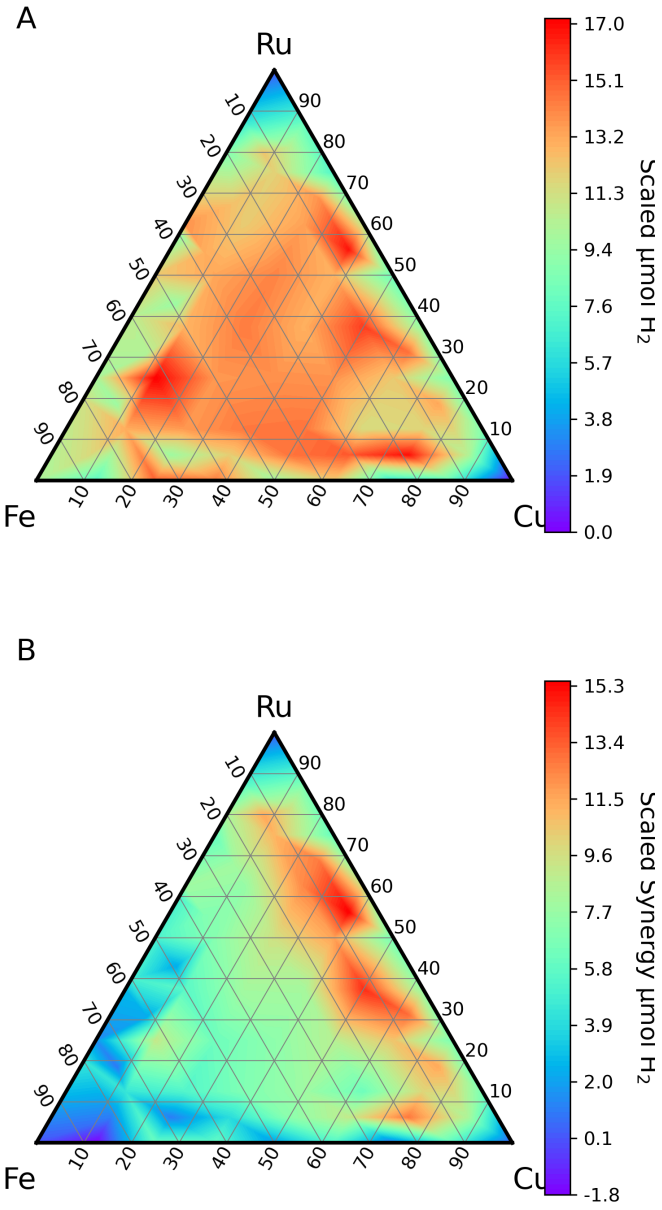

Fig. 5 A. Activity of the ternary data of Cu, Ru, and Fe in μmol H_2. The red points are highly active and the blue points are inactive. The ternary system is consistently more active than the binaries along the axis boundaries. B. Synergies of the ternary data where red is more positive synergies and blue is negative synergies.

and slightly higher Cu concentrations, the highest region of activity is achieved. The highest single composition activity was achieved at 0.1 mM Cu, 0.2 mM Ru, 0.5 mM Fe or a metal ratio of 0.125/0.25/0.625 Cu/Ru/Fe. The data in Figure 5 shows regions with high activity tends to be closer to the center of the ternary, and lower activity are in the corners especially when the sample is Ru rich.

It is evident in Figure 5 B that not only bimetallic but also trimetallic systems tested here have positive synergies. This again, indicates that there is a constructive interaction between Cu, Ru, and Fe for HER where the combination of the three metals is better than the sum of individual populations of Cu, Ru, and Fe at their respective metal concentrations.

3.3.2 Characterizations of ternary metal nanoparticles

TEM micrographs were taken from a sampling of active ternary wells (containing Cu, Ru, and Fe at various concentrations and molar ratios, Figure 6 A). Size historgrams for these samples can be found in Figure S4. STEM-EDS analysis was performed on the highest performing of these wells containing 0.4, 0.1, and 0.3 mM of Cu, Ru, and Fe respectively (Figure 6 B).

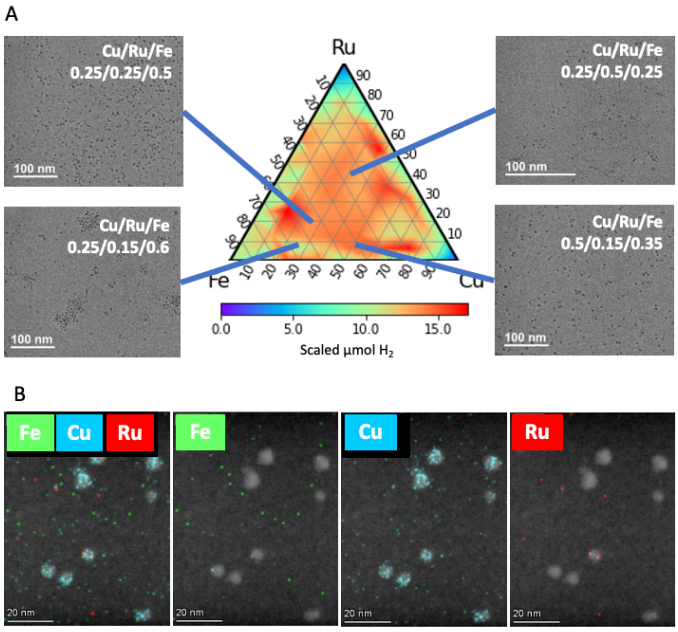

Fig. 6 A. TEM micrographs of four ternary combinations. Sample labels show the molar ratio of metals added to the reaction well. Particles are discrete in all samples. B. STEM-EDS maps of a sample containing 0.4 mM, 0.1 mM, and 0.3 mM Cu, Ru, and Fe respectively. See Figure S9 B for linescan analysis.

The ternary system consistently shows discrete and monodisperse particles (Figure 6 A) by TEM(TEM micrographs are labeled by the molar ratios of metals added to the reaction well). Figure 6 B shows the HAADF images with overlayed STEM-EDS maps of the most active ternary system corresponding to the bottom right TEM micrograph in Figure 6 A. The STEM-EDS maps show that the particles are predominantly Cu containing (see Figure S8 B for linescan analysis). The linescans in Figure S8 B confirm the presence of Cu and CuFe particles. Interestingly, the CuFe particles in the presence of Ru have lower Fe signals as compared to the CuFe particles without the presence of Ru (Figure 4 B). Despite this, the ternary system reported higher activity than the CuFe system.

We found that the wells with the highest HER activity do not contain nanoparticles of uniform composition; rather, they contain particles with a distribution of compositions - CuFe and Cu. Given the heterogeneity within a single sample, we were unable to determine which composition(s) contribute the most to catalytic activity. Nevertheless, this data demonstrates that a ternary combination of metals is unambiguously higher in activity than the individual or binary combinations of the constituent metals.

4 Conclusions

In this work we identified active and colloidally stable multimetallic combinations of Cu, Ru, and Fe as catalysts for photo-driven HER. Within the bimetallic sampling, CuRu, CuFe, and RuFe were all active. In most cases, when we subtracted out the HER activity contributions from the monometallics, the bimetallics outperformed the monometallics, demonstrating positive synergistic interactions in the bimetallic materials. For the Cu and Ru system, Cu and Ru are both relatively inactive for HER, but together the bimetallic combination is highly active for HER indicating a synergistic interaction between the metals. The particles in this system were well defined and determined to have a core-shell CuRu-Cu morphology. For the Cu and Fe system, Cu is relatively inactive while Fe is active, and together, the bimetallic combination forms discrete particles which outperform the pure metals. Two particle populations were observed by STEM-EDS: Cu monometallic particles and CuFe bimetallic particles. For the Ru and Fe system, Ru is inactive while Fe is active, and the bimetallic combination forms discrete particles that outperform the pure metals. The presence of both Ru and Fe in the particles was determined through STEM-EDS mapping.

This study also uncovered a new active ternary catalyst for photo-driven HER. The CuRuFe combination is highly active for HER and, at some concentrations, is significantly better than the monometallic or bimetallic combinations of the same metals. There are regions of high synergies at the lower Fe regimes. The CuRuFe samples analyzed contained predominantly Cu particles. Further study is necessary to identify the origin of the positive synergy in this ternary system.

The identification of a heterogeneous distribution of particle compositions in these 4 multimetallic system with high activity for H_2 evolution highlights the expansive catalytic screening capabilities of this system in contrast to traditional catalytic selection processes. This discovery was enabled by the high-throughput approach used in this work, which allowed for active catalysts with new metal combinations and compositions to be found. Additionally, this study highlights some of the inherent difficulties which arise when correlating composition and metal mixing in multimetallic systems with HER activity when NPs are formed in situ. Even when two metal salts are combined in solution, the addition of a third metal salt can dramatically change the composition of formed particles, further complicating the interpretation of the results. One reason for this difficulty is the discrepancy between

the molar ratio of metals added to the well and the stoichiometry and chemical ordering of the resulting NPs. Despite the compositional variation within the samples, this study conclusively found promising catalysts for photo-driven H_2 production.

Conflicts of interest

There are no conflicts to declare.

Acknowledgements

This research was supported by the U.S. Department of Energy, Office of Science, Office of Basic Energy Sciences, Data Science for Knowledge Discovery for Chemical and Materials Research program, under Award DESC0020392.

Notes and references

1 Z. Sun, Q. Yue, J. Li, J. Xu, H. Zheng and P. Du, *Journal of Materials Chemistry A*, 2015, **3**, 10243–10247.
2 R. Singh and S. Dutta, *Fuel*, 2018, **220**, 607–620.
3 Z.-X. Yang, X.-G. Li, Q.-L. Yao, Z.-H. Lu, N. Zhang, J. Xia, K. Yang, Y.-Q. Wang, K. Zhang, H.-Z. Liu, L.-T. Zhang, H.-J. Lin, Q.-J. Zhou, F. Wang, Z.-M. Yu and J.-M. Ma, *Rare Metals*, 2022, **41**, 3251–3267.
4 A. T. Hoang, A. Pandey, W.-H. Chen, S. F. Ahmed, S. Nižetić, K. H. Ng, Z. Said, X. Q. Duong, Ü. Ağbulut, H. Hadiyanto and X. P. Nguyen, *ACS Sustainable Chemistry amp; Engineering*, 2023, **11**, 1221–1252.
5 Y.-J. Xu, *Frontiers in Catalysis*, 2021, **1**, 708319.
6 E. D. Cline and S. Bernhard, *CHIMIA International Journal for Chemistry*, 2009, **63**, 709–713.
7 E. M. Lopato, E. A. Eikey, Z. C. Simon, S. Back, K. Tran, J. Lewis, J. F. Kowalewski, S. Yazdi, J. R. Kitchin, Z. W. Ulissi, J. E. Millstone and S. Bernhard, *ACS Catalysis*, 2020, **10**, 4244–4252.
8 R. N. Motz, E. M. Lopato, T. U. Connell and S. Bernhard, *Inorganic Chemistry*, 2021, **60**, 774–781.
9 M. Kirch, J.-M. Lehn and J.-P. Sauvage, *Helvetica Chimica Acta*, 1979, **62**, 1345–1384.
10 I. N. Mills, J. A. Porras and S. Bernhard, *Accounts of Chemical Research*, 2018, **51**, 352–364.
11 Q. Yang, M. Dong, H. Song, liu Cao, Y. Zhang, L. Wang, P. Zhang and Z. Chen, *Journal of Materials Science: Materials in Electronics*, 2017, **28**, 10073–10080.
12 J. Zhu, L. Hu, P. Zhao, L. Y. S. Lee and K.-Y. Wong, *Chemical Reviews*, 2019, **120**, 851–918.
13 M. Elvington, J. Brown, S. M. Arachchige and K. J. Brewer, *Journal of the American Chemical Society*, 2007, **129**, 10644–10645.
14 P. N. Curtin, L. L. Tinker, C. M. Burgess, E. D. Cline and S. Bernhard, *Inorganic Chemistry*, 2009, **48**, 10498–10506.
15 T. Kawawaki, Y. Mori, K. Wakamatsu, S. Ozaki, M. Kawachi, S. Hossain and Y. Negishi, *Journal of Materials Chemistry A*, 2020, **8**, 16081–16113.
16 S. Cao, C.-J. Wang, G.-Q. Wang, Y. Chen, X.-J. Lv and W.-F. Fu, *RSC Advances*, 2020, **10**, 5930–5937.
17 M. Bhat, E. M. Lopato, Z. C. Simon, J. E. Millstone, S. Bernhard and J. R. Kitchin, *Reaction Chemistry & Engineering*, 2022, **7**, 599–608.
18 Z. C. Simon, E. M. Lopato, M. Bhat, P. J. Moncure, S. M. Bernhard, J. R. Kitchin, S. Bernhard and J. E. Millstone, *ChemCatChem*, 2021, **14**, nil.
19 E. M. Lopato, S. Talledo, S. DiLuzio, V. Mdluli, Z. C. Simon, K. M. McHugh, J. E. Millstone and S. Bernhard, *ACS Sustainable Chemistry amp; Engineering*, 2022, **10**, 14248–14261.
20 J. K. Nørskov, T. Bligaard, A. Logadottir, J. R. Kitchin, J. G. Chen, S. Pandelov and U. Stimming, *Journal of The Electrochemical Society*, 2005, **152**, J23.
21 P. Du and R. Eisenberg, *Energy & Environmental Science*, 2012, **5**, 6012.
22 A. B. Laursen, A. S. Varela, F. Dionigi, H. Fanchiu, C. Miller, O. L. Trinhammer, J. Rossmeisl and S. Dahl, *Journal of Chemical Education*, 2012, **89**, 1595–1599.
23 J. Yang, H. Yan, X. Zong, F. Wen, M. Liu and C. Li, *Philosophical Transactions of the Royal Society A: Mathematical, Physical and Engineering Sciences*, 2013, **371**, 20110430.
24 C.-J. Wang, S. Cao, B. Qin, C. Zhang, T.-T. Li and W.-F. Fu, *ChemSusChem*, 2014, **7**, 1924–1933.
25 M. Zeng and Y. Li, *Journal of Materials Chemistry A*, 2015, **3**, 14942–14962.
26 P. C. K. Vesborg, B. Seger and I. Chorkendorff, *The Journal of Physical Chemistry Letters*, 2015, **6**, 951–957.
27 C. Li and J.-B. Baek, *ACS Omega*, 2019, **5**, 31–40.
28 A. Kumar and S. Deka, *Applied Catalysis A: General*, 2020, **599**, 117575.
29 Y. Liu, Z. Sun and Y. H. Hu, *Chemical Engineering Journal*, 2021, **409**, 128250.
30 N. E. Motl, E. Ewusi-Annan, I. T. Sines, L. Jensen and R. E. Schaak, *The Journal of Physical Chemistry C*, 2010, **114**, 19263–19269.
31 R. He, Y.-C. Wang, X. Wang, Z. Wang, G. Liu, W. Zhou, L. Wen, Q. Li, X. Wang, X. Chen, J. Zeng and J. G. Hou, *Nature Communications*, 2014, **5**, 4327.
32 M. B. Gawande, A. Goswami, F.-X. Felpin, T. Asefa, X. Huang, R. Silva, X. Zou, R. Zboril and R. S. Varma, *Chemical Reviews*, 2016, **116**, 3722–3811.
33 J. Durst, C. Simon, A. Siebel, P. J. Rheinländer, T. Schuler, M. Hanzlik, J. Herranz, F. Hasché and H. A. Gasteiger, *ECS Transactions*, 2014, **64**, 1069–1080.
34 O. Inderwildi, S. Jenkins and D. King, *Surface Science*, 2007, **601**, L103–L108.
35 Z. Cui, S. Duan, S. Yao, T. Pan, D. Dai and H. Gao, *ChemElectroChem*, 2021, **8**, 705–711.
36 R. F. Zhang, X. F. Kong, H. T. Wang, S. H. Zhang, D. Legut, S. H. Sheng, S. Srinivasan, K. Rajan and T. C. Germann, *Scientific Reports*, 2017, **7**, 9577.
37 M. Bhavanari, K.-R. Lee, C.-J. Tseng, I.-H. Tang and H.-H. Chen, *International Journal of Hydrogen Energy*, 2021, **46**, 35886–35895.
38 L. Zhou, D. F. Swearer, C. Zhang, H. Robatjazi, H. Zhao,

L. Henderson, L. Dong, P. Christopher, E. A. Carter, P. Nordlander and N. J. Halas, *Science*, 2018, **362**, 69–72.

39 Q. Wu, M. Luo, J. Han, W. Peng, Y. Zhao, D. Chen, M. Peng, J. Liu, F. M. F. de Groot and Y. Tan, *ACS Energy Letters*, 2019, **5**, 192–199.

40 X. Mao, L. Wang, Y. Xu, P. Wang, Y. Li and J. Zhao, *npj Computational Materials*, 2021, **7**, 46.

41 T. Qiu, Z. Liang, W. Guo, S. Gao, C. Qu, H. Tabassum, H. Zhang, B. Zhu, R. Zou and Y. Shao-Horn, *Nano Energy*, 2019, **58**, 1–10.

42 A. M. Huerta-Flores, F. Ruiz-Zepeda, C. Eyovge, J. P. Winczewski, M. Vandichel, M. Gaberšček, N. D. Boscher, H. J. Gardeniers, L. M. Torres-Martínez and A. Susarrey-Arce, *ACS Applied Materials amp; Interfaces*, 2022, **14**, 31767–31781.

43 A. Soto-Arreola, A. M. Huerta-Flores, J. Mora-Hernández and L. M. Torres-Martínez, *Journal of Photochemistry and Photobiology A: Chemistry*, 2018, **357**, 20–29.

44 R. Cheng, X. Fan, M. Wang, M. Li, J. Tian and L. Zhang, *RSC Advances*, 2016, **6**, 18990–18995.

45 S. Renukadevi and A. P. Jeyakumari, *Journal of Materials Science: Materials in Electronics*, 2021, **32**, 25399–25408.

46 G. Zhang, W. Zhang, D. Minakata, Y. Chen, J. Crittenden and P. Wang, *International Journal of Hydrogen Energy*, 2013, **38**, 11727–11736.

47 H. Li, Q. Tang, B. He and P. Yang, *Journal of Materials Chemistry A*, 2016, **4**, 6513–6520.

48 Y. Wei, X. Zhang, Y. Liu, C. Jia and P. Yang, *Electrochimica Acta*, 2020, **349**, 136366.

49 A. Juliya, V. A. Mujeeb, K. Sreenivasan and K. Muraleedharan, *Journal of Photochemistry and Photobiology*, 2021, **8**, 100076.

50 E. M. Lopato and S. Bernhard, *Energy & Fuels*, 2021, **35**, 18957–18981.

51 W. Song, E. M. Lopato, S. Bernhard, P. A. Salvador and G. S. Rohrer, *Applied Catalysis B: Environmental*, 2020, **269**, 118750.

52 S. Adhikari, T. Bhattacharjee, S. Bhattacharjee, C. G. Daniliuc, A. Frontera, E. M. Lopato and S. Bernhard, *Dalton Transactions*, 2021, **50**, 5632–5643.

53 S. Wang, D. Zhong, Y. Xu and N. Zhong, *New Journal of Chemistry*, 2021, **45**, 13969–13978.

54 M. Bhat and J. Kitchin, *gespyranto*, 2021, https://doi.org/10.5281/zenodo.5525144.

55 K. Sağır, H. Elçiçek and O. K. Özdemir, *International Journal of Hydrogen Energy*, 2021, **46**, 5689–5698.